Dynamic Characteristics of Gear Coupling and Rotor System in Transmission Process Considering Misalignment and Tooth Contact Analysis

Authors:

Wei Fan, Hong Lu, Yongquan Zhang, Xiangang Su

Abstract:

> The dynamic vibration of the gear coupling-rotor system (GCRS) caused by misalignment is an important factor of low frequency vibration and noise radiation of the naval marine. The axial misalignment of gear coupling is inevitable owing to mass eccentricity, and is unconstrained in axial direction at high-speed operation. Therefore, the dynamic model of GCRS is proposed, considering gear-coupling misalignment and contact force in this paper. The whole motion differential equation of GCRS is established based on the finite element method. Moreover, the numerical calculation method of meshing force, considering the uniform distribution load on contact surface, is presented, and the mathematical predictive time?frequency characteristics are analyzed by the Newmark stepwise integral approach. Finally, a reduced-scale application of the propulsion shaft system is utilized to validate the effectiveness of the proposed dynamic model. For the sensibility to low-frequency vibration, the natural frequencies and vibration modes of GCRS are analyzed through the processing and analysis of acceleration signal. The experimental dynamic response and main components of vibration are respectively consistent with mathematical results, which demonstrate the effectiveness of the proposed dynamic model of GCRS with misalignment. Furthermore, it also shows that the proposed finite element analysis and calculation method are suitable for complex shafting, providing a novel thought for dynamic analysis of the propeller?shaft?hull coupled system of marine.

Record Type: Published Article

Dynamic Characteristics of Gear Coupling and Rotor System in Transmission Process Considering Misalignment and Tooth Contact Analysis

Wei Fan [1],*[ID], **Hong Lu** [2][ID], **Yongquan Zhang** [2][ID] **and Xiangang Su** [2]

[1]   School of Engineering, Huazhong Agricultural University, Wuhan 430070, China
[2]   School of Mechanical and Electronic Engineering, Wuhan University of Technology, Wuhan 430070, China;
     landzh@whut.edu.cn (H.L.); zhangyongquan@whut.edu.cn (Y.Z.); sxg@whut.edu.cn (X.S.)
*   Correspondence: fanwei@mail.hzau.edu.cn; Tel.: +86-159-7210-0910

Abstract: The dynamic vibration of the gear coupling-rotor system (GCRS) caused by misalignment is an important factor of low frequency vibration and noise radiation of the naval marine. The axial misalignment of gear coupling is inevitable owing to mass eccentricity, and is unconstrained in axial direction at high-speed operation. Therefore, the dynamic model of GCRS is proposed, considering gear-coupling misalignment and contact force in this paper. The whole motion differential equation of GCRS is established based on the finite element method. Moreover, the numerical calculation method of meshing force, considering the uniform distribution load on contact surface, is presented, and the mathematical predictive time–frequency characteristics are analyzed by the Newmark stepwise integral approach. Finally, a reduced-scale application of the propulsion shaft system is utilized to validate the effectiveness of the proposed dynamic model. For the sensibility to low-frequency vibration, the natural frequencies and vibration modes of GCRS are analyzed through the processing and analysis of acceleration signal. The experimental dynamic response and main components of vibration are respectively consistent with mathematical results, which demonstrate the effectiveness of the proposed dynamic model of GCRS with misalignment. Furthermore, it also shows that the proposed finite element analysis and calculation method are suitable for complex shafting, providing a novel thought for dynamic analysis of the propeller–shaft–hull coupled system of marine.

Keywords: gear coupling-rotor system; misalignment; dynamic characteristics; finite element analysis; low-frequency vibration

1. Introduction

The gear coupling-rotor system (GCRS) is a common mechanical component used extensively to transfer motion and torsion in drive systems. For its higher load carrying capacity than other forms of flexible couplings, the GCRS is applied in a wide range of applications, including marine, aerospace, manufacturing, and wind power. Figure 1a shows gear coupling, which is used as a kind of aircraft emergency power system to drive the turbine and turn generator by ram air. As shown in Figure 1b, the propulsion shaft system, which uses the rotation of the GCRS to output the power by the generator to the propeller–shaft–hull, is an important power system of the naval marine. To ensure stable and smooth running of the GCRS during sailing, the low-frequency vibration acoustic radiation and dynamic response of the GCRS are essential to study.

(**a**)   (**b**)

Figure 1. The industry application of gear coupling-rotor system (GCRS). (**a**) Application in the ram air turbine of aerospace. (**b**) Application in the propulsion shaft system.

However, the dynamic characteristics of GCRS (an important power transmission system in propulsion shaft system) are critically influenced by the misalignment of gear coupling. Gear coupling consists of two key components: internal gear sleeve and external gear hub. The hub is an external gear that has longitude involute and tip sphere teeth and the sleeve has internal teeth. The two components compose a special gear pair. The difference compared to other types of internal gear pairs is that the number of external gear hub teeth is the same as the number of internal gear sleeve teeth. The rotational motion and torsional moment can be transmitted from the generator to the propeller by the engagement of gear coupling. Due to the manufacturing and assembly error, deformation of shaft body, thrust and vibration disturbance, and the change of environment and temperature, the perfect alignment condition of the two axes will inevitably worsen. The misalignment condition accounts for approximately 20% of the known failures of GCRS. Therefore, to optimize performance of the propulsion shaft system, it is important to investigate tooth contact analysis under load distribution and study the dynamic characteristics of the GCRS when the involute gear coupling is working with misalignment.

Numerous researches have been performed for meshing tooth contact analysis with misalignment. Cuffaro [1] found that the stiffness may affect both load and pressure distribution along tooth surface. Zhao [2] established the three dimensional (3D) model and conducted the finite element analysis of ship gear coupling with misalignment, and finally drew the conclusion that the contact pressure can vary in the different meshing area of tooth. Guan [3] developed a computational contact analysis finite element model to determine the contact points for gear coupling. Tan [4] made research about the distribution of contact pressure of teeth under the circumstance of radial and angular misalignment using the finite element method only. Besides the finite element method, Al-Hussain [5] proposed the motion differential equation of gear coupling by the Lagrange method, which takes into account the parallel misalignment and angle misalignment separately in the potential energy equation. Barrot [6] indicated that the correct approximation of tooth stiffness is essential to analyze the pressure distribution, and even a little difference in the determination of meshing force may cause a significant variation in the dynamics. Hong [7] established a hybrid analytical-computational model. The tooth compliance caused by bending, shear, contact, and torsion was solved computationally, which can inspire us in the contact stiffness analysis.

For the dynamic analysis of whole GCRS, the research has two kinds of main paradigms: transfer matrix method [8] and finite element method. Tian [9] investigated the mode shapes, dynamic response, and critical speed of revolution of the whole shaft system. The study results indicate that the severe vibration of GCRS can be motivated with the offset of the axes of rotational components, and the vibration frequency is equivalent to the lateral natural frequency. Kim [10] and Huang [11] used the transfer matrix to establish the dynamic model and conduct the natural

characteristics analysis. The characteristics of the harmonic component were reviewed through the steady-state response and mode shape type. The transfer matrix is more suitable for the simplified structure model. Guo [12] presented a meshing force model by finite element method and studied the evolution rule of the meshing force with different misalignment. M.L. [13] and Lei [14] derived the dynamic model of the rotor-gear coupling system by the finite element method. They found that the second harmonic component is more prominent, and the radial force can cause the lateral vibration with multiple frequency components.

Although many scholars have extensive research for the dynamics of GCRS, the existing study is still inadequate. The contact state between sleeve and hub is normally simplified as point contact or line contact, nevertheless, the actual meshing process is surface contact, the variation and distribution of meshing pressure on the contact area with misalignment warrants more research. Moreover, most of the researches mainly focus on the parallel offset of the two axes of the external gear hub and internal gear sleeve, the GCRS is affected by both parallel and angular misalignment. The dynamic response of GCRS influenced by comprehensive factors, such as misalignment and bearing stiffness, need to be further analyzed.

This paper is organized as follows: Section 2 presents the modeling and analysis of GCRS. The motion differential equation of GCRS is established by the finite element method. The local meshing force and global induced loads of gear coupling are analyzed, considering both parallel and angular misalignment. The motion differential equation of GCRS is solved by the subspace iteration method and Newmark stepwise integration method in Section 3. Furthermore, the effects of misalignment of gear coupling and bearing stiffness on the time–frequency dynamic response of GCRS are analyzed. In Section 4, the dynamic characteristics test experiment is carried out, whose software system is developed based on Virtual Instrument Technology. The dynamic response and first four natural frequency are detected and analyzed. Besides, the effectiveness of comprehensive meshing force for gear coupling and dynamic model for GCRS is verified through comparing the result of the mathematical analysis model and experimental test. Conclusions are drawn in Section 5.

2. Modeling and Analysis of GCRS

In this section, the dynamic differential equation of GCRS is proposed by using the finite element method. Then, the generating principles, geometries, and dynamics of gear coupling are investigated. Moreover, the mathematical meshing force model with misalignment for contact dynamic response analysis is proposed, as well as the contact force model, considering bearing stiffness.

2.1. Finite Element Model of GCRS

The configuration of the GCRS is shown in Figure 2a. The involute tooth coupling which is mounted to connect the motor and shaft, is designed to contain allowable misalignment and backlash.
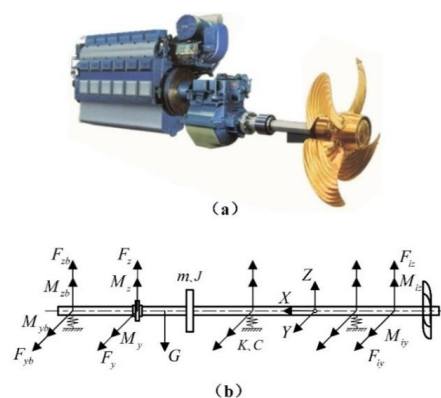

(a)

(b)

Figure 2. Configuration of ship power system. (**a**) The physical structure of propulsion shaft system. (**b**) The diagram model of GCRS.

Based on the finite element numerical analysis method, the GCRS can be discretized into non-uniform cantilever elements as shown in Figure 2b. Assuming that the GCRS contains n nodes, F_{iz} and M_{iz} are the force and moment of the ith node in z-axis, and F_{iy} and M_{iy} are the force and moment of the ith node in y-axis, respectively. F_{zb}, M_{zb}, F_{yb}, and M_{yb} are the force and moment in z-axis and y-axis of the node where gear coupling located. m and J are the mass and inertia of the flywheel. K and C are the stiffness and damp of bearings. F_{zb}, M_{zb}, F_{yb}, and M_{yb} are the force and moment in z-axis and y-axis of the node where bearing located, respectively.

For any node of the GCRS, the translational and angular displacement will be generated in both the y-axis and z-axis direction. The displacement vectors of each node of GCRS are defined as:

$$u = \begin{bmatrix} y_i & z_i & -\theta_{y_i} & \theta_{z_i} \end{bmatrix}^T \tag{1}$$

where y_i and z_i are the translational displacements of ith node in the horizontal and vertical direction. θ_{y_i} and θ_{z_i} are the angular displacements of ith node in the horizontal and vertical direction, respectively.

According to the Euler–Bernoulli beam model, the dynamic differential equation of GCRS can be expressed as [15]:

$$[M]\{\ddot{u}\} + ([C] - [J]\Omega)\{\dot{u}\} + [K]\{u\} = Q(t) + G + F(u, \dot{u}, t) + F(u, t) \tag{2}$$

where M and J are the equivalent mass and rotational inertia matrices, C and K are the damp and stiffness matrices, $Q(t)$ and G are the unbalance force and gravity. $F(u, \dot{u}, t)$ and $F(u, t)$ are the force vector of bearing supports and comprehensive force of gear coupling.

The GCRS can be divided into several nodes and elements. The equivalent concentrated external force on each node is defined as nodal force. The virtual work of equivalent nodal force of node e can be expressed as:

$$\Delta V = (\{\delta^*\}^e)^T \{F\}^e \tag{3}$$

where $\{\delta^*\}^e$ is the virtual displacement of node e.

The virtual strain energy caused by internal strain of node e can be expressed as:

$$\Delta U = (\{\delta^*\}^e)^T \iiint [B]^T \{\sigma\} dx dy dz \tag{4}$$

where $[B]$ is the strain matrix.

Since the virtual strain energy is equal to the virtual work induced by external force, the following equation can be obtained:

$$(\{\delta^*\}^e)^T \{F\}^e = (\{\delta^*\}^e)^T \iiint [B]^T \{\sigma\} dx dy dz \tag{5}$$

Then, the nodal force can be obtained:

$$\{F\}^e = \iiint [B]^T \{\sigma\} dx dy dz \tag{6}$$

where $\{\sigma\} = [D][B]\{\delta\}^e$ is the stress. (6) can be rewritten as:

$$\{F\}^e = \{\delta\}^e \iiint [B]^T [D][B] dx dy dz \tag{7}$$

Hence, the stiffness matrix of each element can be obtained:

$$[k]^e = \iiint [B]^T [D][B] dx dy dz \tag{8}$$

Similarly, the mass matrix of each element can be obtained by virtual work principle:

$$[m]^e = \iiint [N]^T \rho [N] dx dy dz \tag{9}$$

For the linear elastic shaft element, the shape function can be defined as [16]:

$$[N] = \begin{bmatrix} 1 - 3\varsigma^2 + 2\varsigma^3 \\ l(\varsigma - 2\varsigma^2 + \varsigma^3) \\ 3\varsigma^2 - 2\varsigma^3 \\ l(-\varsigma^2 + \varsigma^3) \end{bmatrix}^T \tag{10}$$

where ς is the ratio of the position x to the length l of the shaft element.

Furthermore, the mass matrix can be expressed as:

$$[M_i] = \frac{m_i}{420} \begin{bmatrix} 156 & 22L_i & 54 & -13L_i \\ 22L_i & 4L_i^2 & 13L_i & -3L_i^2 \\ 54 & 13L_i & 156 & -22L_i \\ -13L_i & -3L_i^2 & -22L_i & 4L_i^2 \end{bmatrix} \tag{11}$$

where m_i is the mass of the ith element of the shaft.

According to the stress–strain relationship of materials, the strain matrix of the ith element can be obtained by taking the derivative of the shape function. The stiffness matrix of the ith shaft element can be obtained by numerical integration from (8).

$$[K_i] = \frac{EI_i}{L_i^3} \begin{bmatrix} 12 & 6L_i & -12 & 6L_i \\ 6L_i & 4L_i^2 & -6L_i & 2L_i^2 \\ -12 & -6L_i & 12 & -6L_i \\ 6L_i & 2L_i^2 & -6L_i & 4L_i^2 \end{bmatrix} \tag{12}$$

The gyroscopic matrix can be expressed as:

$$[J_i] = \frac{\mu\kappa}{15L_i} \begin{bmatrix} 36 & 3L_i & -36 & 3L_i \\ 3L_i & 4L_i^2 & -3L_i & -L_i^2 \\ -36 & -3L_i & 36 & -3L_i \\ 3L_i & -L_i^2 & -3L_i & 4L_i^2 \end{bmatrix} \tag{13}$$

In (2), the total stiffness matrix of GCRS is made up of the stiffness of all corresponding discrete nodes. For the node in which the bearing is located on, the node stiffness can be added to the correspondent diagonal elements of stiffness matrix K. However, the node in which the gear coupling is located on will be affected by the dynamic and unbalanced excitation force (the frequency is almost two times the rotational frequency of GCRS) due to the misalignment. The unbalanced exaction force can be expressed as [1]:

$$\begin{cases} F_{yc} = F_y + 2m_c e\omega^2 \sin(2\omega t - 2\varphi_0) \\ F_{zc} = F_z + 2m_c e\omega^2 \cos(2\omega t - 2\varphi_0) \end{cases} \tag{14}$$

where m_c is the mass of the sleeve, ω is the rotational frequency of GCRS. F_y and F_z are the component force of comprehensive meshing force of the gear coupling in y-axis and z-axis, which is distinctly affected by the misalignment. Therefore, the dynamic meshing state and comprehensive meshing force of GCRS with misalignment need to be analyzed.

2.2. Meshing Model of Parallel Misalignment Gear Coupling (PMGC)

To proceed with the analysis of gear coupling with misalignment, two sets of coordinates are established:

1. $\{S^o : O^o - X^o Y^o Z^o\}$: the coordinate of the external gear hub as shown in Figure 2, the z-axis is in the horizontal direction, namely the centerline of the ith teeth, the Y-axis is coincident with the vertical direction, and the origin point O^0 denotes the center point of hub.

2.　　$\left\{ S^i : O^i - X^i Y^i Z^i \right\}$: the coordinate of the internal gear sleeve with parallel misalignment, the z-axis and x-axis are in the same direction of S^0, the origin point O^i denotes the center point of sleeve with offset.

　　As can be seen in Figure 3, the dotted line is the initial position of the ith internal involute teeth when the internal gear sleeve is not offset. C^f is the intersection of the addendum circle of internal gear sleeve with offset and the involute profile of external gear hub. $l_i^{AC_f}$ is the actual mesh arc length in the ith teeth of both hub and sleeve, and $l_i^{AC_f}$ is subdivided into n parts with equal arc length, consequently. A is the point of addendum circle of the external gear hub located on the involute line of the ith internal gear sleeve teeth, and B is the point of addendum circle of the internal gear sleeve located on the involute line of the ith external involute teeth. The arc l_{ij}^{PB} denotes the arc length between the random point P_{ij} located in the meshing arc l_i^{AC} and the root point B. R_{ij} denotes the radius of point P_{ij}. R_a is the distance between point C^f and origin point O^i, namely, the radius of addendum circle of the ith involute teeth of internal gear sleeve. R_c^f is the distance between point C^f and origin point O^0, namely, the radius of point C^f in the ith involute teeth profile of external gear hub.
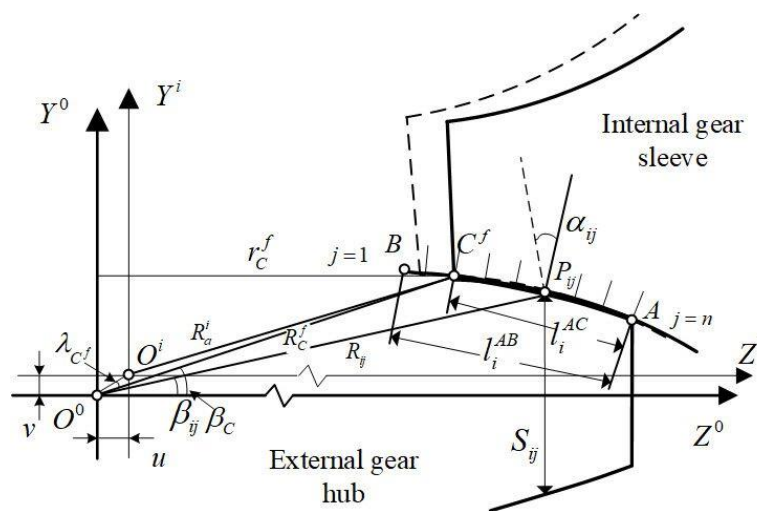

Figure 3. The meshing model of equal division for involute teeth with parallel misalignment.

　　When the axis of the internal gear sleeve and external gear hub is offset, l_i^{AB} (the length of total arc length for the ith involute teeth) and l_i^{AC} (the length of actual meshing line for the ith involute teeth) can be obtained by principle of involute generation:

$$\begin{cases} l_i^{AB} = \dfrac{R_b}{2}\left(\tan^2 \alpha_A - \tan^2 \alpha_B\right) \\ l_i^{AC} = \dfrac{R_b}{2}\left(\tan^2 \alpha_A - \tan^2 \alpha_{Cf}\right) \end{cases} \tag{15}$$

where R_b is the radius of base circle of external hub, $\alpha_A = \arccos(R_b/R_A)$ is the pressure angle at point A (locate on the addendum circle of external gear hub), $\alpha_B = \arccos(R_b/R_B)$ is the pressure angle at point B. (locate on the root circle of external gear hub).

　　To the jth point which is located on the random position of actual meshing arc l_i^{AC}, the geometrical relationship of PMGC can be deduced as:

$$\begin{cases} l_{ij}^{PC} = j\Delta l - l_{ij}^{CB} \\ \alpha_{ij} = \arctan \sqrt{\left(\dfrac{2l_{ij}^{PC}}{R_b} + \tan^2 \alpha_{Cf}\right)} \quad (j = 1, \cdots, n) \\ R_{ij} = \dfrac{R_b}{\cos \alpha_{ij}} \end{cases} \tag{16}$$

Then, the corresponding teeth thickness and teeth angle of P_{ij} can be expressed as:

$$\begin{cases} S_{ij} = \frac{\pi m R_{ij}}{2R_b} - 2R_{ij}\left(inv\alpha_{ij} - inv\alpha\right) \\ \beta_{ij} = \arcsin\left(\frac{S_{ij}}{2R_{ij}}\right) \end{cases} \tag{17}$$

where S_{ij} is the tooth thickness of point P_{ij}.

R_c^f is the distance between point C^f and origin point O^0, namely, the radius of point C^f in the ith involute teeth profile of external gear hub, which can be obtained by the law of cosine:

$$\begin{cases} R_C^f = \left(R_a^{i2} + u^2 + v^2 - 2R_a^{i2}\sqrt{u^2 + v^2}\cos\lambda_i\right)^{0.5} \\ \lambda_i = \frac{\pi}{2} - \arctan\left(\frac{v}{u}\right) - \beta_i \end{cases} \tag{18}$$

where β_{ij} is the angle between R_{ij} and the center line of the ith teeth of hub, and it can be obtained from cosine law:

$$\beta_i = \arctan\left[\frac{S_i}{mz} + inv\alpha - inv\left(\arccos\frac{R_b}{R_C^f}\right)\right] \tag{19}$$

With the solution of the radius of point C_i considering angular misalignment, the regenerative meshing line l_i^{AC}, pressure angle α_{ij} and tooth thickness S_{ij} can be obtained.

2.3. Meshing Model of Angular Misaligned Gear Coupling (AMGC)

When the gear coupling tilts because of angular misalignment, the contact areas on each tooth shift away from the center of the tooth flank. As can be seen in Figure 4, the area *O, I*, and *H* are represented the tooth surface of hub, sleeve, and the meshing area without misalignment. The origin point O^0 is located on the intersection of x-axis and end surface of hub, and the origin point O^i is located on the intersection of x-axis and the central vertical line of sleeve. R_a^o and R_f^o are the addendum radius and root radius of hub. R_a^i and R_f^i are the addendum radius and root radius of sleeve, respectively. B denotes the length of meshing area along with the x-axis.
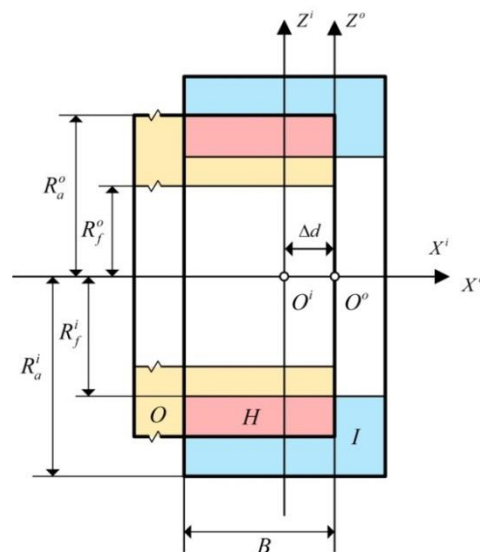

Figure 4. The meshing model of gear coupling without misalignment.

The meshing models of gear coupling in the initial state and with angular misalignment are shown in Figure 5. The divergence of meshing area and contact length will vary with the angular

misalignment. Assuming that there's a micro misaligned rotational angle θ around y-axis, and the angle vertex is located at a distance of L_m away from the Z^i-axis in sleeve coordinate. Simultaneously, the contact tooth surface of the internal hub and external sleeve is also changed. It is clear that the contact tooth surface has become the largest area in the positive direction of Z^i-axis, while it is reduced to the smallest area in the negative direction of Z^i-axis. The contact area of other meshing teeth is a range between them. To facilitate the discussion, the largest contact area in the positive direction of Z^i-axis can be divided into two parts: H_1 and H_2.
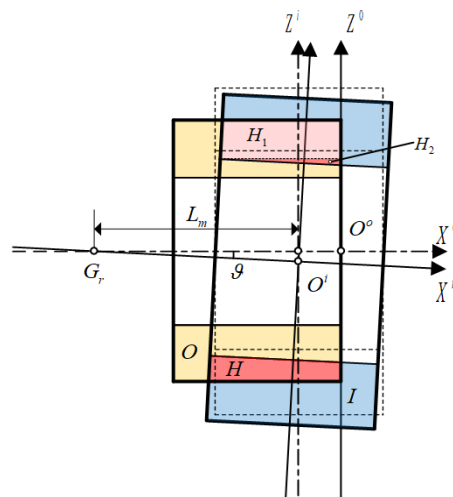

Figure 5. The meshing model of Angular Misaligned Gear Coupling (AMGC).

To facilitate the analysis of numerical relationship between angular misalignment and meshing force, the contact model is shown in Figure 6, in detail. Owing to the small misaligned angle, point C and E_r are the intersection of the addendum circle of sleeve and involute tooth of hub. In the actual meshing situation, the intersection of the sleeve and the involute tooth moves from point A to point C at the right end surface of the hub. D is the point that has equal radius with the point E_r, and b_D is the contact width in the X^i-axis. Then, the projection length of the radius of C and D on Z^i-axis can be deduced as:

$$\begin{cases} r_C = \frac{r_a^i}{\cos\theta} - (L + \Delta d)\tan\theta \\ r_D = \frac{r_a^i}{\cos\theta} - 2\left(L + r_a^i \tan\vartheta\right)\tan\frac{\theta}{2} \\ b_D = (L + \Delta d)\tan\theta - 2\left(L + r_a^i \tan\theta\right)\tan\frac{\theta}{2} \end{cases} \tag{20}$$

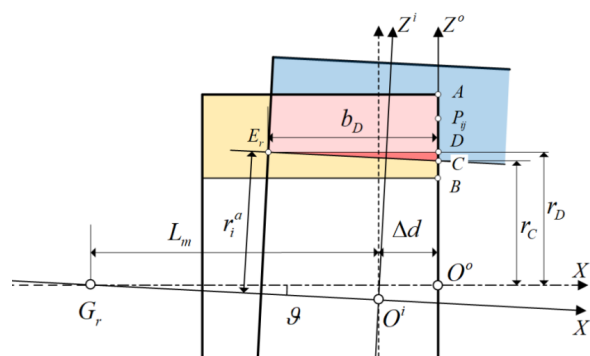where r_a^i is the radius of addendum circle of internal gear sleeve.

Figure 6. Analysis of the contact area of AMGC in the positive direction of z-axis.

The projection length of the radius of C and D on Z^0-axis on random teeth can be expressed as:

$$\begin{cases} r_{iC} = r_b + (r_C - r_b)|\sin\varphi_i| \\ r_{iD} = r_b + (r_D - r_b)|\sin\varphi_i| \end{cases} \tag{21}$$

where $\sin\varphi_i$ is presented to compensate the contact error for insufficient contact.

$$b_{ij} = \begin{cases} (r_{ij} - r_C)\tan\theta & P_{ij} \text{ located in } H_1 \\ (r_{ij} - r_C)\tan\theta - \dfrac{2(r_{ij} - r_D)}{\sin(2\theta)} & P_{ij} \text{located in } H_2 \end{cases} \tag{22}$$

The following equations can be obtained by transform the coordinate XOZ into coordinate YOZ:

$$\begin{cases} R_C^f = \dfrac{r_c}{\cos\beta_c} \\ \beta_c = \arcsin\left[\dfrac{\pi m}{2R} + inv\alpha - inv\left(\arccos\left(\dfrac{R_b}{R_C}\right)\right)\right] \\ \varphi_i = \dfrac{\pi}{2} + \arctan\left(\dfrac{v}{u}\right) + \lambda_a + \beta_a \end{cases} \tag{23}$$

where R is the radius of pitch circle of involute tooth. R_c^f is the radius of point C located in the coordinate of external gear hub, which can be calculated by substituting (20) and (21) in (23) based on Newton iteration method.

2.4. The Comprehensive Meshing Force Model of Gear Coupling with Misalignment

Considering the basal-deformation and shearing-deformation transmitted to the driveline, the load induced elastic deformation of individual tooth can be divided into the following three categories based on the Weber Energy method as shown in Figure 7: (1) the deformation δ^s caused by bending, shear, and axial compression at involute tooth; (2) deformation δ^b at the round corners and basal body; (3) local contact deformation δ^c caused by contact stress. The deformation caused by contact stress in the jth part is equal to the deformation caused by forces when q is big enough.
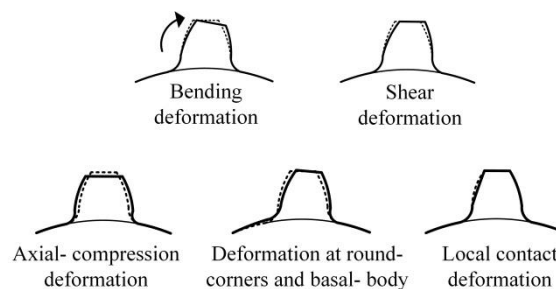

Figure 7. The contact deformation of involute teeth.

In the contact surface, with the variation of load position, the meshing parameters, such as pressure angle, tooth thickness, and misaligned characteristics, are different, although, in the same contact load and stress, the elastic deformation of the above mentioned three types are different. As shown in Figure 8, the uniform distributed load is defined as q, L_i is the length of the cantilever, L_{ij} is the distance between the load point P_{ij} and the supporting point of cantilever, L_{kj} is the distance between P_{ij} and the kth element.
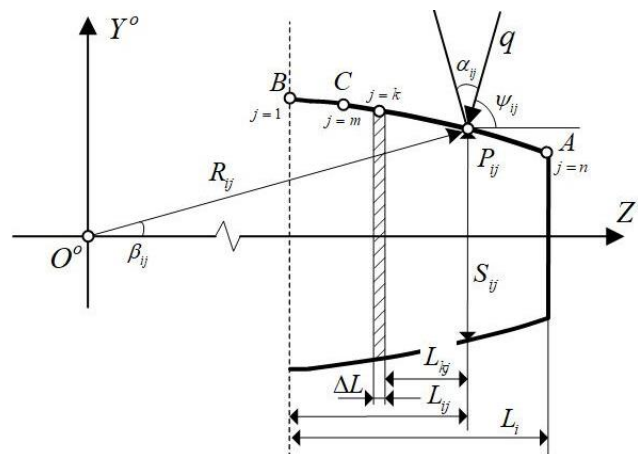
Figure 8. The model of equal division for meshing deformation.

Approximately, the *k*th tiny arc of meshing tooth profile can be presumed as the length of ΔL, the geometrics can be obtained:

$$\begin{cases} \Delta L = \Delta l \\ L_i = R_a \cos \beta_a - R_f \cos \beta_f \\ L_{ij} = R_{ij} \cos \beta_{ij} - R_f \cos \beta_f \\ L_{kj} = R_{ij} \cos \beta_{ij} - R_{ik} \cos \beta_{ik} - \Delta L \end{cases} \tag{24}$$

where β is the angle between the radius of some point located on the tooth profile and *Z*-axis.

The total deformation δ of the *j*th part in the *i*th involute teeth can be expressed as [17]:

$$\delta_{ij} = \sum_{j=m}^{j=n} \sum_{k=m}^{k=j} \left(\delta_{jk}^s + \delta_{jk}^b + \delta_{jk}^c \right) \tag{25}$$

where

$$\begin{cases} \delta_{jk}^s = \frac{12 q \Delta L (1+v) \cos^2 (\alpha_{ij} - \beta_{ij})}{5 E_e A_k} \\ \delta_{jk}^b = \frac{q \Delta L \sin^2 (\alpha_{ij} - \beta_{ij})}{E_e A_k} \\ \delta_{jk}^c = \frac{q \Delta L \cos (\alpha_{ij} - \beta_{ij})}{20 E_e I_k} \left[4 \left(\Delta L^2 + 3 L_{jk} \Delta L + 3 L_{jk}^2 \right) \cos (\alpha_{ij} - \beta_{ij}) - 5 S_{ij} (\Delta L + 2 L_{jk}) \sin (\alpha_{ij} - \beta_{ij}) \right] \end{cases} \tag{26}$$

where E_e and v are elasticity modulus and Poisson ratio, I_k and A_k are the inertia moment and cross-section area of *k*th element.

The theoretical tooth stiffness has been calculated by the ratio between the applied uniform load and the load induced deformation of the *j*th part for the *i*th teeth by considering the tooth as a cantilever beam.

$$K_j = \frac{q}{\delta_j^b + \delta_j^s + \delta_j^c} \tag{27}$$

Therefore, the comprehensive meshing stiffness of the tooth pair obtained can be expressed as:

$$K = \frac{\sum q}{\delta^b + \delta^s + \delta^c} \tag{28}$$

The comprehensive meshing force model consists of torsional force and dynamic force. During the meshing process, the torque load transmitted by the engaged teeth is called torsional force, and the force caused by the vibration displacement is called dynamic force. Hence, the normal force between a pair of involute teeth can be obtained as:

$$T = \sum_{i=1}^{i=Z} T_i = \sum_{i=1}^{i=Z} \sum_{j=m'}^{j=n} T_{ij} = \sum_{i=1}^{i=Z} \sum_{j=m'}^{j=n} \left[q_{ij} R_{ij} \cos(\alpha_{ij} - \beta_{ij}) \right] \tag{29}$$

where T is the transmitted torque, and T_{ij} is the transmitted torque of jth part in the ith teeth.

The load on each tooth is distributed into n slices along the face width direction. Since the torsional angular displacement of each tooth relative to the root is equal, the meshing force caused by torsion of jth slice in the ith teeth is expressed as:

$$q_{ij} = K_{ij}\chi_{ij} = \frac{\phi K_{ij}(R_{ij} - R_f)}{\cos(\alpha_{ij} - \beta_{ij})} \tag{30}$$

Substitute (29) into (30), the torsional angular displacement can be obtained:

$$\phi = \frac{T}{\sum\limits_{i=1}^{i=Z} \sum\limits_{j=m'}^{j=n} K_{ij} R_{ij} (R_{ij} - R_f)} \tag{31}$$

The meshing force caused by torsion of the jth slice for the ith teeth can be rewritten as:

$$q_{ij} = \frac{T K_{ij}(R_{ij} - R_f)}{\cos(\alpha_{ij} - \beta_{ij}) \sum\limits_{i=1}^{i=Z} \sum\limits_{j=m'}^{j=n} K_{ij}(R_{ij} - R_f) R_{ij}} \tag{32}$$

The meshing force caused by the vibration displacement of the jth slice for the ith teeth is defined as:

$$f_{ij} = \frac{K_{ij}\sqrt{u_y^2 + v_z^2}\sin\theta_i}{\cos(\alpha_{ij} - \beta_{ij})} \tag{33}$$

Hence, the comprehensive meshing force on each slice can be obtained as:

$$\begin{aligned} F_{ij} &= q_{ij} + f_{ij} \\ &= \frac{K_{ij}}{\cos(\alpha_{ij} - \beta_{ij})} \left[\frac{T(R_{ij} - R_f)}{\sum\limits_{i=1}^{i=Z} \sum\limits_{j=m'}^{j=n} K_{ij}(R_{ij} - R_f) R_{ij}} + \sqrt{u_y^2 + v_z^2}\sin\varphi_i \right] \end{aligned} \tag{34}$$

The comprehensive meshing force is variable in the different slice of the teeth, and the individual teeth force cannot be calculated by the sum of each slice. According to the four quadrants in the

coordinate of external gear hub, the comprehensive meshing force can be decomposed in the y and z-axis. The comprehensive meshing force of individual teeth can be expressed as:

$$
\begin{cases}
F_{iy} = \sum\limits_{j=m}^{j=n} F_{ij} \cos\psi_{ij} = \sum\limits_{j=m}^{j=n} \dfrac{K_{ij}\cos\psi_{ij}}{\cos(\alpha_{ij}-\beta_{ij})} \left[\dfrac{T(R_{ij}-R_f)}{\sum\limits_{i=1}^{i=Z}\sum\limits_{j=m'}^{j=n} K_{ij}(R_{ij}-R_f)R_{ij}} + \sqrt{u_y^2+v_z^2}\sin\theta_i \right] \\[4mm]
F_{iz} = \sum\limits_{j=m}^{j=n} F_{ij} \sin\psi_{ij} = \sum\limits_{j=m}^{j=n} \dfrac{K_{ij}\sin\psi_{ij}}{\cos(\alpha_{ij}-\beta_{ij})} \left[\dfrac{T(R_{ij}-R_f)}{\sum\limits_{i=1}^{i=Z}\sum\limits_{j=m'}^{j=n} K_{ij}(R_{ij}-R_f)R_{ij}} + \sqrt{u_y^2+v_z^2}\sin\theta_i \right]
\end{cases}
\tag{35}
$$

where ψ_{ij} is the angle between the normal direction of the *j*th tooth profile and the positive direction of *z*-axis.

The (35) can be rewritten as:

$$
\begin{cases}
F_y = \sum\limits_{i=1}^{i=Z} F_{iy} = \sum\limits_{i=1}^{i=Z}\sum\limits_{j=m}^{j=n} F_{ij}\cos\psi_{ij} \\[4mm]
F_z = \sum\limits_{i=1}^{i=Z} F_{iz} = \sum\limits_{i=1}^{i=Z}\sum\limits_{j=m}^{j=n} F_{ij}\sin\psi_{ij}
\end{cases}
\tag{36}
$$

2.5. The Dynamic Model of Ball Bearing

According to the Hertz contact theory, the contact force between ball and raceway of both inner and outer rings is considered to be the point contact. The contact model of the individual point contact between *j*th ball and groove is shown in Figure 9. $d_m/2$ is the distance between the *j*th ball and center point of bearing. δ_{ji} is the contact deformation of *j*th ball. R_b is the radius of the ball. R_i is the radius of the raceway of inner ring. O_c is the center point of the actual contact ellipse, and a_i and b_i are the length of long and short axis.
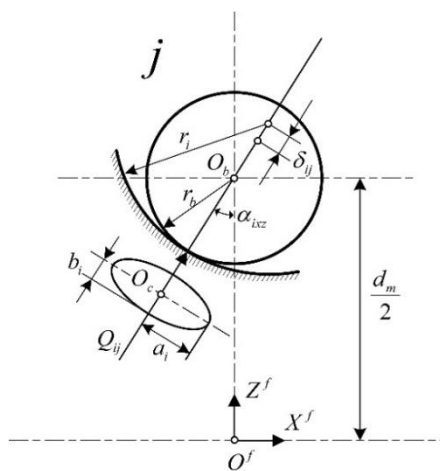

Figure 9. The contact model of ball bearing.

The normal contact load of ball bearing can be expressed as [18]:

$$
\begin{cases}
Q_{ji} = K_{ji}\delta_{ji}^{1.5} \\[2mm]
K_{ji} = \dfrac{\pi\kappa E_{ave}}{3F}\left(\dfrac{2E}{F\Sigma\rho}\right)^{0.5} \\[2mm]
\delta_{ji} = \left| (r_i - r_b) - l_{jibr}^f \right|
\end{cases}
\tag{37}
$$

where K_{ji} is the deformation coefficient of the *j*th ball, E_{ave} is the average elastic modulus, κ *and* $\sum \rho$ are the eccentricity ratio and curvature.

The contact force of the whole bearing can be obtained by integration:

$$
\begin{cases}
F_{yb} = -C_b \dot{y} + \sum\limits_{j=1}^{j=Z} \left(Q_{jiy}^i \right) \\
F_{zb} = -C_b \dot{z} + \sum\limits_{j=1}^{j=Z} \left(Q_{jiz}^i \right)
\end{cases}
\tag{38}
$$

where $C_b = 1.0 \times 10^{-5} K_{ji} \delta_{ji}^{0.5}$ is the contact damp [19].

By Substituting (36) and (38) into (9) and (2), the unbalanced exaction force can be obtained. Moreover, the dynamic response of GCRS is analyzed by solving the motion differential equation in Section 3.

3. Dynamic Response Analysis and Test of GCRS

3.1. Numerical Calculation Method of GCRS

To investigate the influence of gear coupling misalignment and rotor speed on the time–frequency response of gear coupling-rotor system, the subspace iterative method is used to divide and analyze the GCRS units, and the Newmark stepwise integral approach is adopted to solve the differential equation of GCRS

As can be seen in Figure 10a, the simplified GCRS is mainly composed of the motor, gear-coupling, bearings, shaft, and propeller. The shaft is supported by four bearings, which are installed in a specified location. For the infinite degrees of freedom of GCRS, the equivalent mass and moment of inertia are concentrated on the left and right nodes along the shaft axis (the nodes are generally set at the location of sudden change of shaft radius or special parts). Then, each shaft element can be simplified as a massless uniform elastic shaft, and the GCRS is resolved into a limited degree of freedom system. All nodes and elements are numbered consecutively from motor to the propeller, as shown in Figure 10b. The gear coupling is located on node 3, and the bearings are spread on nodes 6, 9, 13, 16, respectively. The parameters of the adopted gear coupling are shown in Table 1, and the node and element parameters are listed in Table 2.
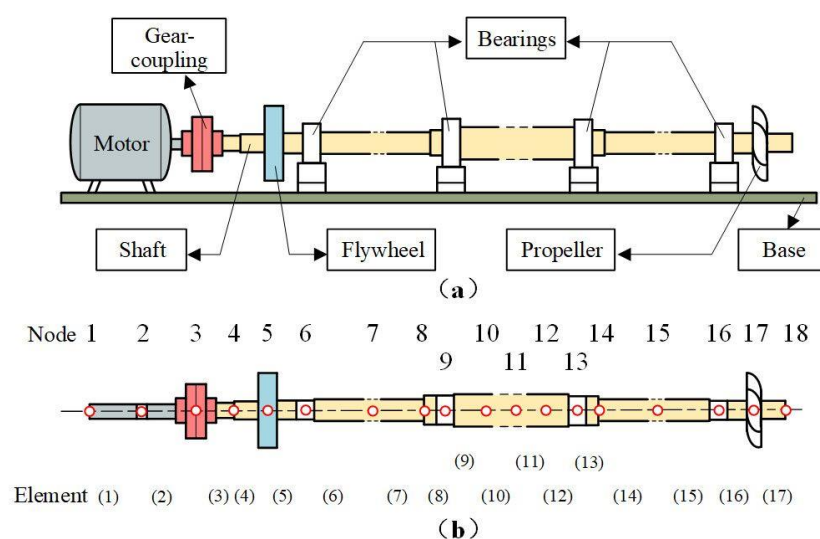

Figure 10. Structure diagram of GCRS. (**a**) Configuration of GCRS. (**b**) Diagram of nodes and elements spread.

Table 1. Basic structure parameters of adopted gear coupling.

Components	Modulus	Number of Teeth	Tooth Width (mm)	Inner Diameter (mm)	Outer Diameter (mm)	Pressure Angle (°)
External gear hub	1.25	20	25	16	27.49	20
Internal gear sleeve	1.25	20	30	23.44	34	20

Table 2. Nodes and elements of GCRS.

Parameters of Elements				Parameters of Nodes		
Number	Length (mm)	Diameter (mm)	Mass(kg)	Number	Additional Diameter (mm)	Additional Mass (kg)
				1		
1	100	26	0.419	2		
2	40	24	0.143	3		
3	50	20	0.124	4		
4	43	22	0.129	5	200	5.879
5	51	24	0.182	6		
6	132	28	0.642	7		
7	120	28	0.583	8		
8	31	30	0.173	9		
9	114	34	0.817	10		
10	105	34	0.753	11		
11	105	34	0.753	12		
12	114	34	0.817	13		
13	31	30	0.173	14		
14	120	28	0.583	15		
15	132	28	0.642	16		
16	51	24	0.182	17	100	2.561
17	43	22	0.129	18		

The numerical calculation process is achieved by using the Newmark stepwise integration method. The initial rotational speed is set to 1000 r/min. The acceleration in next Δt is set to 1 m/s². The iterative formula of the classical Newmark method to solve the dynamic response in this paper:

$$\{\dot{x}_{k+1}\}_{t+\Delta t} = \{\dot{x}\}_t + \Delta t[(1-\gamma)\{\ddot{x}_t\} + \gamma \ddot{x}_{t+\Delta t}]$$
$$\{x_{k+1}\}_{t+\Delta t} = \{x\}_t + \Delta t^2[(\tfrac{1}{2} - \beta)\{\ddot{x}_t\} + \beta \ddot{x}_{t+\Delta t}]$$

(39)

where h is the time step, $\beta = 0.25$ and $\gamma = 0.5$ are the initial control parameter. The greater the value of β, the more stability the system is. When $\beta > 0.125$ and $\frac{\Delta t}{T} \leq \frac{1}{2\pi \sqrt{\beta}}$, the system converges to a stable state. The calculation process is achieved by MATLAB. The initial velocity and acceleration are set to 1000 r/min and 1 m/s², respectively.

The continuous time domain is divided into several discrete time intervals Δt. The initial t_i denotes that the first contact point can be obtained. Then, the meshing points that satisfy the constraints of dynamic Equation (9) can be solved by using the Newmark numerical method. After that, the dynamic response has been calculated in one subdivision angular displacement. Assume that the support of the motor shaft is rigid. To proceed with the numerical computation and experimental test of dynamic response, the key node numbers 7, 11, and 15 are adopted to analyze.

3.2. Mathematical Solution and Analysis of the Dynamic Response of GCRS

For the initial state, the GCRS is set to operate without misalignment. In Figure 11, the time–frequency domain dynamic response of the key nodes in *y*-axis and *z*-axis is shown in Figure 11a,b. The steady state

dynamic responses of adopted nodes in the y-axis are $\pm 0.25 \times 10^{-4}$ m, $\pm 0.55 \times 10^{-4}$ m, $\pm 0.8 \times 10^{-4}$ m, and $\pm 1.0 \times 10^{-4}$m. Meanwhile, the steady state dynamic responses of adopted nodes in the z-axis are $\pm 0.85 \times 10^{-4}$ m, $\pm 0.75 \times 10^{-4}$ m, $\pm 0.65 \times 10^{-4}$ m, $\pm 0.74 \times 10^{-4}$ m. The comparative results indicate that the steady value of dynamic response in the y-axis is larger than in the z-axis, which means that the system has higher stability in the z-axis than in the y-axis. Moreover, the bearing stiffness is set to 5 Nm in Figure 10, and 2 Nm in Figure 12. The amplitude of steady value is extended both in the z-axis and y-axis as the bearing stiffness decreases, while the stability time is not changed, which means that improving the bearing stiffness can effectively reduce the transient response of vibration.
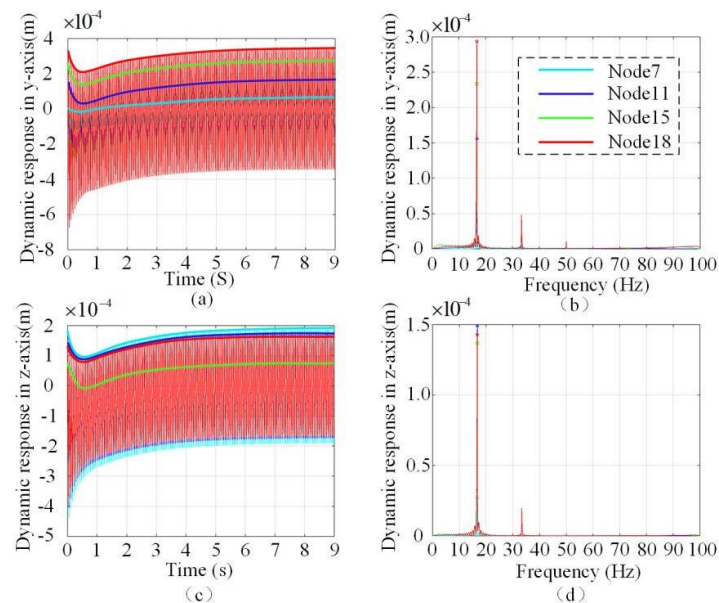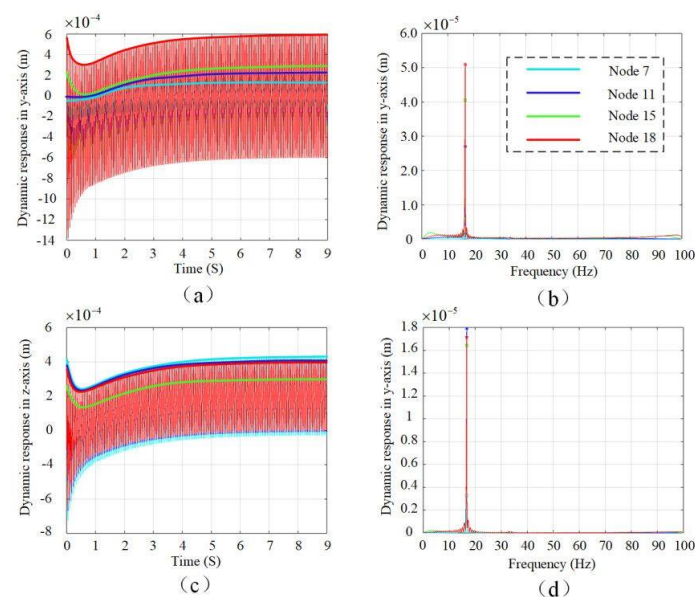

Figure 11. The dynamic response of GCRS with the bearing stiffness of 5 Nm. (**a**) The time domain dynamic response in the y-axis. (**b**) The frequency domain dynamic response in the y-axis. (**c**) The time domain dynamic response in the z-axis. (**d**) The time domain dynamic response in the z-axis.

Figure 12. The dynamic response of GCRS with the bearing stiffness of 2 Nm. (**a**) The time domain dynamic response in the y-axis. (**b**) The frequency domain dynamic response in the y-axis. (**c**) The time domain dynamic response in the z-axis. (**d**) The time domain dynamic response in the z-axis.

From Figures 13 and 14, the effects of parallel and angular misalignment on the dynamic response of GCRS are investigated by mathematical model. The angular misalignment between the hub and sleeve is denoted by θ, and the parallel misalignment is denoted by a. Figure 13 shows the dynamic response of node 7, 11, and 15 in y-axis and z-axis with $\theta = 0.5°$ and $a = 0.4$ mm misalignment. As can be seen from Figure 13a–f, the second harmonic generation is motivated in both the y-axis and z-axis of the number 7, 11, and 15 nodes. The vibration amplitude is gradually reduced as the distance between nodes and gear coupling increasing. Figure 14 shows the dynamic response of nodes 7, 11, and 15 in the y-axis and z-axis with $\theta = 0.5°$ and $a = 0.8$ mm misalignment. As the parallel misalignment increases, the first and second harmonic vibration amplitude becomes higher, the third and fourth harmonic generation components also emerge. Figure 15 shows the dynamic response of nodes 7, 11, and 15 in the y-axis and z-axis with $\theta = 0.2°$ and $a = 0.4$ mm misalignment. The second harmonic generation can be dramatically reduced by the decrease of angular misalignment. Moreover, from Figures 13–15, the mathematical simulated results show that the parallel and angular misalignment have implications on the damp and inertia force, which will give rise to the second harmonic components and amplify the vibration amplitude in both the y-axis and z-axis.
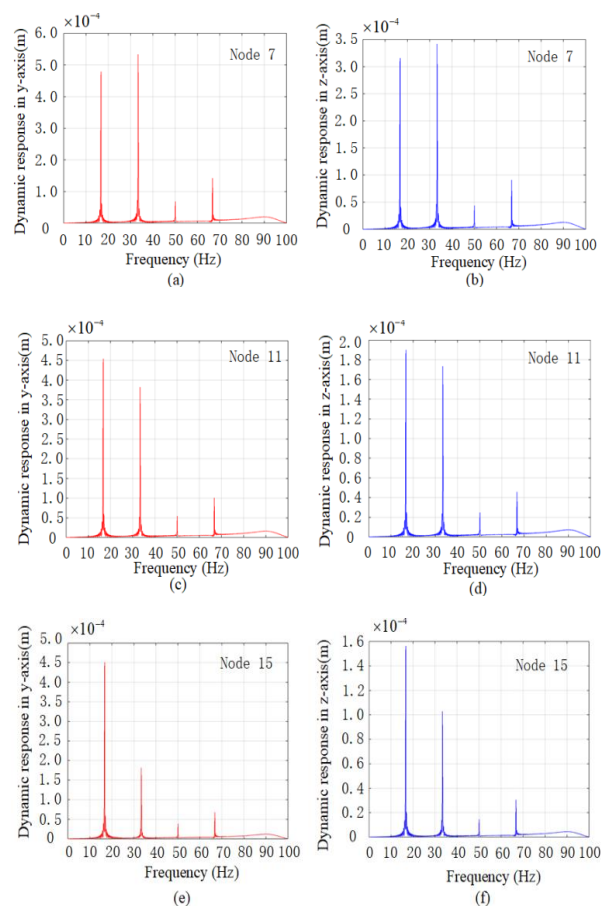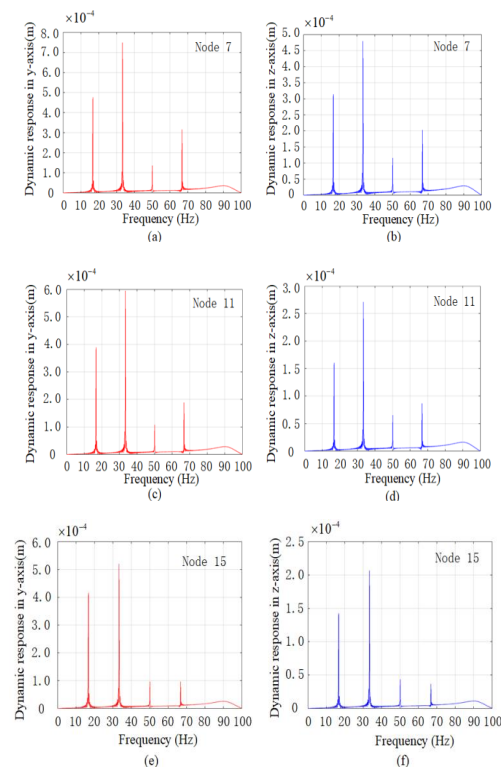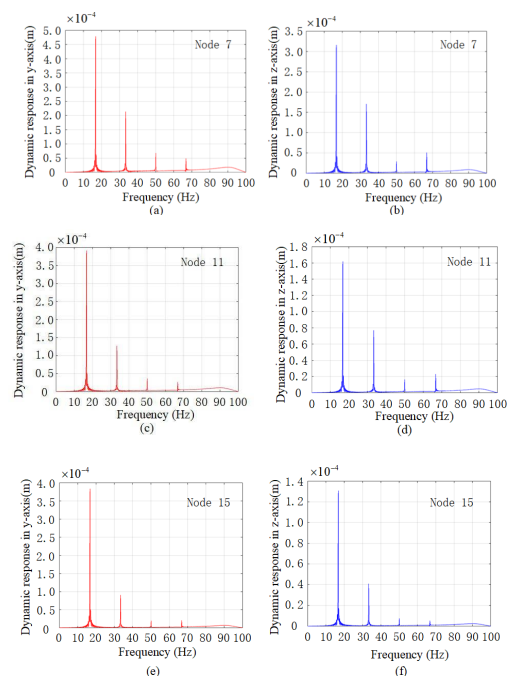

Figure 13. The mathematical simulated dynamic response with 0.4 mm parallel misalignment and 0.5° angular misalignment of nodes 7, 11, and 15 in the y-axis and z-axis. (**a**) Node 7 in the y-axis. (**b**) Node 7 in the z-axis. (**c**) Node 11 in the y-axis. (**d**) Node 11 in the y-axis. (**e**) Node 15 in the y-axis. (**f**) Node 15 in the z-axis.

Figure 14. The mathematical simulated dynamic response with 0.8 mm parallel misalignment and 0.5° angular misalignment of nodes 7, 11, and 15 in the *y*-axis and *z*-axis. (**a**) Node 7 in the *y*-axis. (**b**) Node 7 in the *z*-axis. (**c**) Node 11 in the *y*-axis. (**d**) Node 11 in the *y*-axis. (**e**) Node 15 in the *y*-axis. (**f**) Node 15 in the *z*-axis.

Figure 15. The mathematical simulated dynamic response with 0.4 mm parallel misalignment and 0.2° angular misalignment of nodes 7, 11, and 15 in the *y*-axis and *z*-axis. (**a**) Node 7 in the *y*-axis. (**b**) Node 7 in the *z*-axis. (**c**) Node 11 in the *y*-axis. (**d**) Node 11 in the *y*-axis. (**e**) Node 15 in the *y*-axis. (**f**) Node 15 in the *z*-axis.

4. Experimental Dynamic Characteristics Analysis of GCRS

In order to verify the proposed comprehensive meshing force model, the comparison experiments are carried out on the industry rotational shaft system in this section. In the experiment, the tri-axial acceleration sensor is selected to collect the vibration signal, and the dynamic performance test of GCRS was conducted by the eddy current sensor and National Instruments (NI) vibration monitoring analyzer as shown in Figure 16. The hammer is used to simulate with a 3 Hz test bandwidth. A data acquisition (DAQ) card inserted in a PC is used to receive the analog signal. All of the AD/DA conversion, system memory allocation, and accessing modules are executed by the controller of NI. The detection data is analyzed by the LabVIEW frequency response analyzer code.
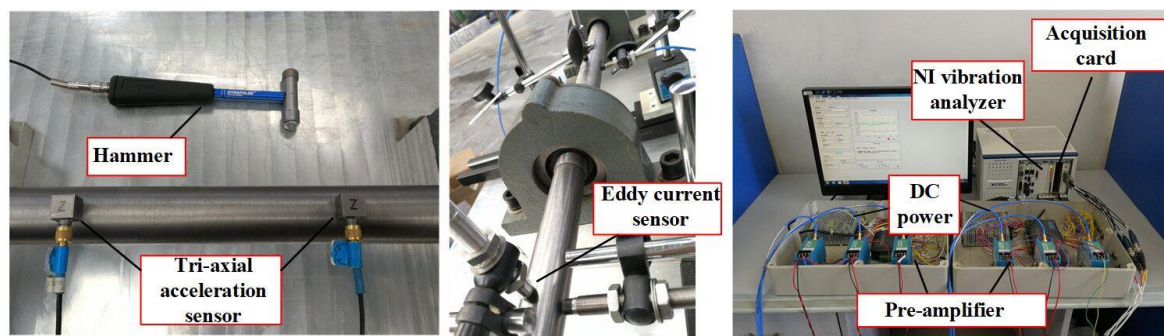

Figure 16. The dynamic response experiment setup of GCRS.

The rotational speed can be set from 0 to 3000 r/min. The dynamic response signal of nodes 7, 11, 15 can be obtained by tri-axial acceleration and vibration detection. According to sampling theorem $f_s > 2f_m$, the sampling frequency is 1000 Hz in order to ensure the reliability of the experimental data. The vibration voltage signal $\{a(k)\}$ ($k = 0, 1, 2,..., N$, where N is the number of samples) collected by acceleration sensor is converted into acceleration signal with unit conversion, then the time domain signal in Figure 17a can be obtained. After the separation of trend term and noise signal by Infinite Impulse Response (IIR) digital filter, the time characteristic curve can be obtained in Figure 17b. In order to obtain displacement signals, the acceleration signal needs to be integrated through twice trapezoidal integral formula $y(k) = \Delta t \sum_{i=1}^{k} \left[a_{(i-1)} + a_{(i)} \right]/2$. Finally, the frequency characteristic curve can be obtained by Discrete Fourier Transform (DFT) $Y(k) = \sum_{r=0}^{N-1} y(r)e^{-j2\pi kr/N}$. Figure 17b shows the original time domain signal curve and time domain characteristic curve after trend term elimination, respectively. Figure 18c shows the first four natural frequencies by DFT of GCRS.
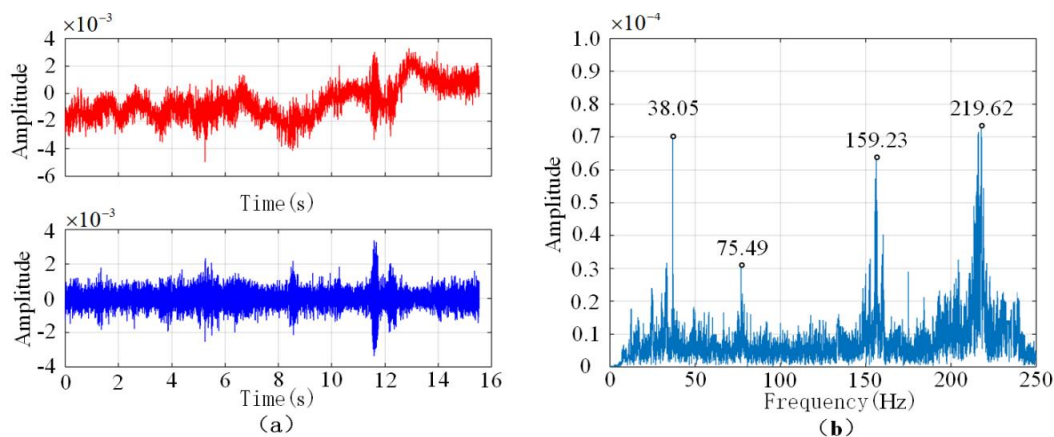

Figure 17. The time–frequency characteristic curve of GCRS. (**a**) The original acceleration signal. (**b**) The frequency characteristic curve.
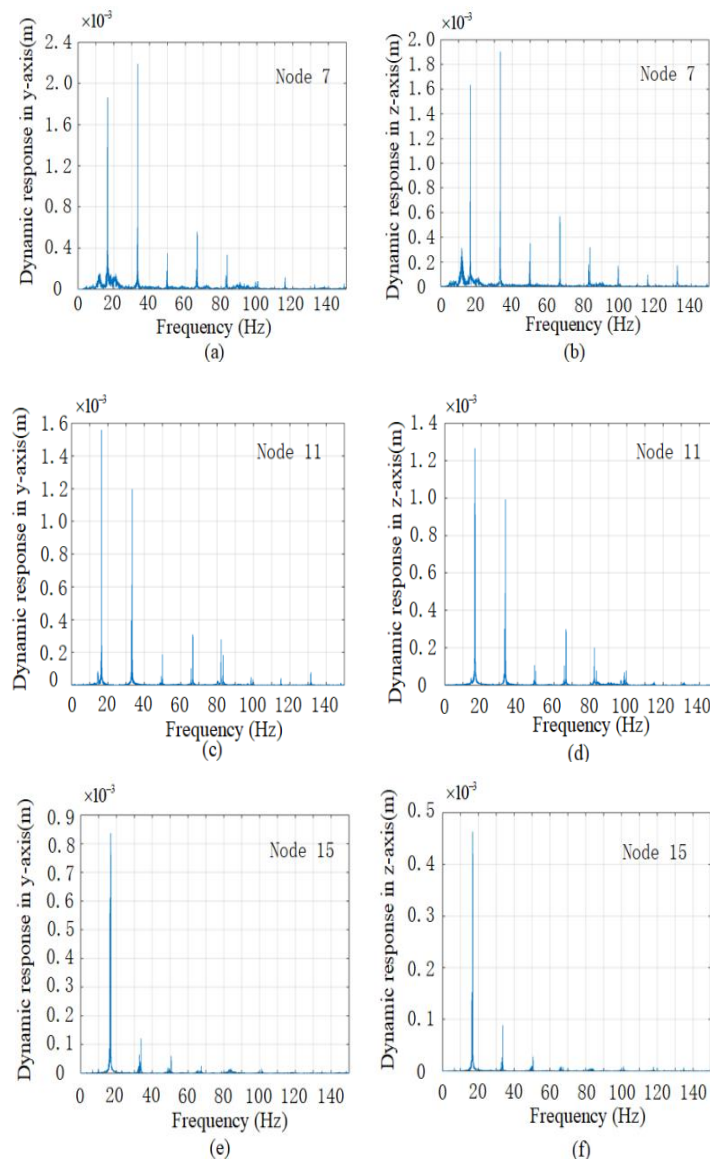
Figure 18. The experimental dynamic response with 0.4 mm parallel misalignment and 0.5° angular misalignment of nodes 7, 11, and 15 in the y-axis and z-axis. (**a**) Node 7 in the y-axis. (**b**) Node 7 in the z-axis. (**c**) Node 11 in the y-axis. (**d**) Node 11 in the y-axis. (**e**) Node 15 in the y-axis. (**f**) Node 15 in the z-axis.

To proceed with the experimental test of parallel and angular misalignment of gear coupling, the standard feeler gauges with different thicknesses are placed under the bearing supports. The value of angular misalignment is determined by the distance and height difference of bearing supports, which is ensured by the measurement of dial indicator. The sample frequency is set to 300 Hz, and the dynamic response of nodes 7, 11, and 15 are obtained from Figures 18–20.
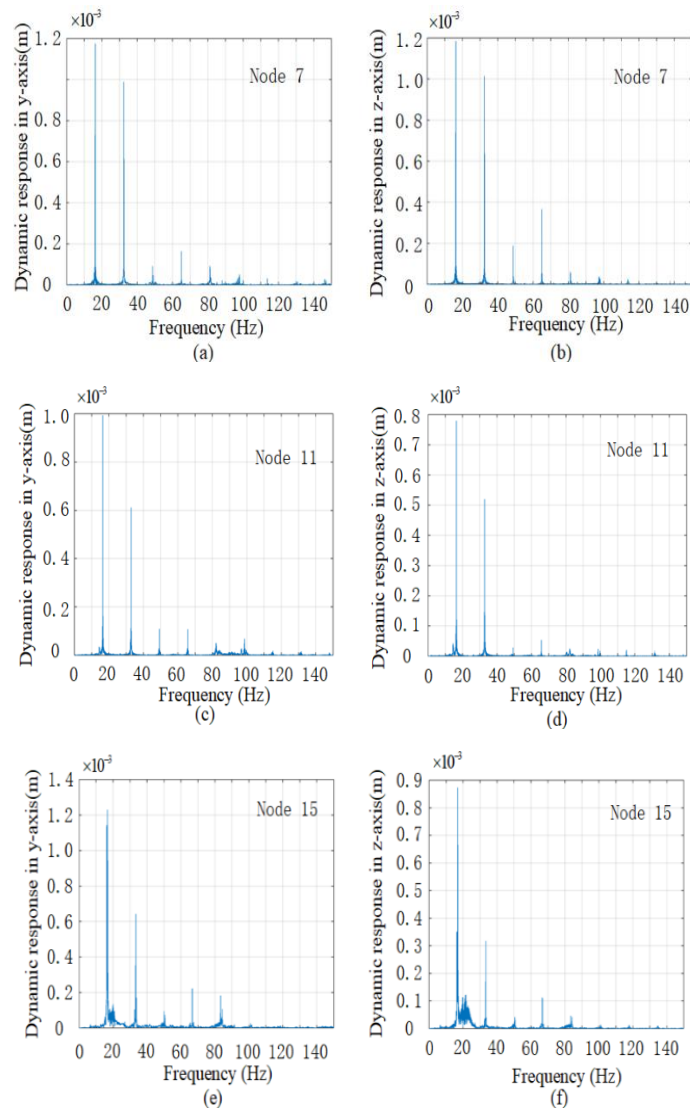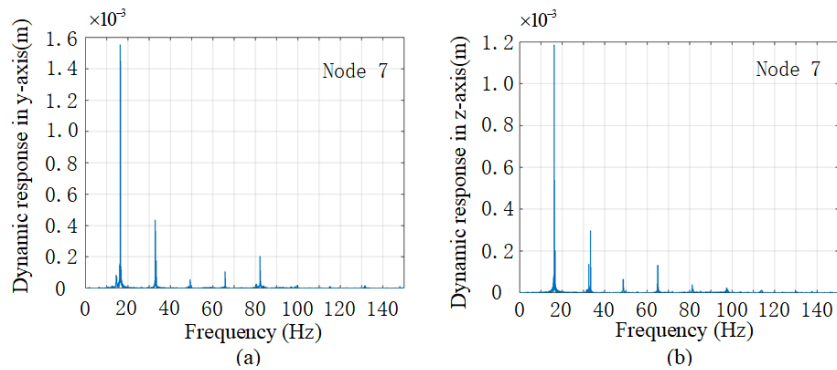
Figure 19. The experimental dynamic response with 0.8 mm parallel misalignment and 0.5° angular misalignment of nodes 7, 11, and 15 in the y-axis and z-axis. (**a**) Node 7 in the y-axis. (**b**) Node 7 in the z-axis. (**c**) Node 11 in the y-axis. (**d**) Node 11 in the y-axis. (**e**) Node 15 in the y-axis. (**f**) Node 15 in the z-axis.
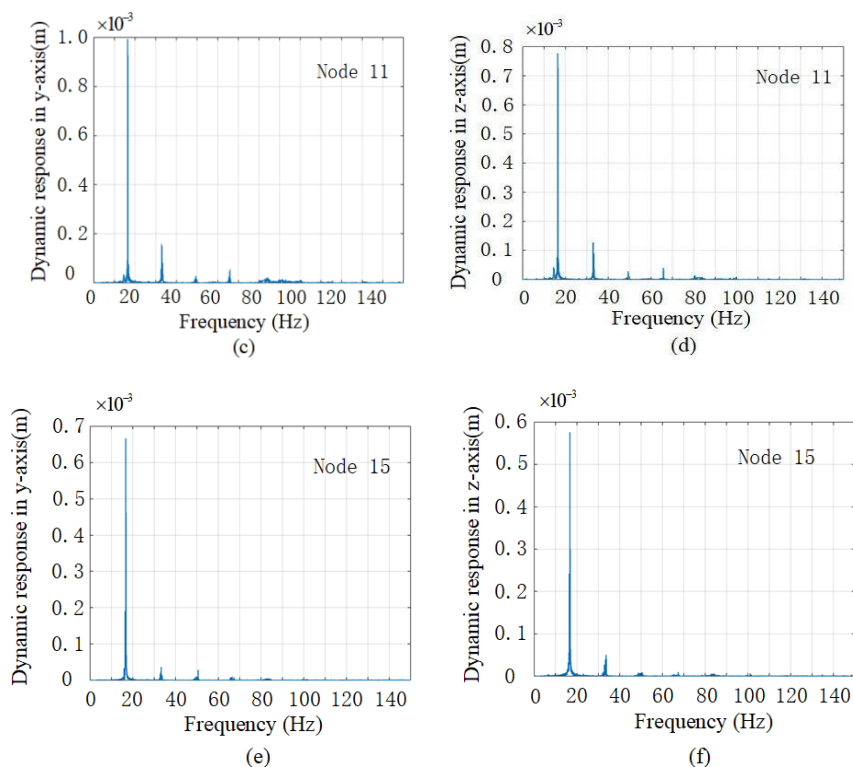

Figure 20. *Cont.*

Figure 20. The experimental dynamic response with 0.4 mm parallel misalignment and 0.2° angular misalignment of nodes 7, 11, and 15 in *y*-axis and *z*-axis. (**a**) Node 7 in *y*-axis. (**b**) Node 7 in *z*-axis. (**c**) Node 11 in *y*-axis. (**d**) Node 11 in *y*-axis. (**e**) Node 15 in *y*-axis. (**f**) Node 15 in *z*-axis.

From the experimental results of the dynamic response curves from Figures 18–20, it can be seen that, the variation trend and rule of each order harmonic generations are consistent with that in the mathematical model. In comparison to the *z*-axis, the experimental results indicate that the magnitude of dynamic response in the *y*-axis is larger than that in the *z*-axis, which confirms that the GCRS is more stable in vertical direction than in horizon direction. In Figure 18, the GCRS is operated with 0.4 mm parallel misalignment and 0.5° angular misalignment. The second harmonic generation can be obviously detected in nodes 7, 11, and 15 in both the *y*-axis and *z*-axis. The amplitude of second harmonic generation of the nodes which is closer to the gear coupling is much higher, which means the influence of misalignment is reduced as the distance away from gear coupling increases. Besides the second harmonic generation, the third and fourth harmonic generation components emerge, as well as some low amplitude high order integer harmonic generations. The experimental dynamic response curves with 0.8 mm parallel misalignment and 0.5° angular misalignment of nodes 7, 11, and 15 are shown in Figure 19. The second harmonic generations become more obvious as the parallel offset increases, and the third, fourth, and even some high order harmonic generations have been generated in the location close to the gear coupling. Figure 20 shows dynamic response curves with 0.4 mm parallel misalignment and 0.2° angular misalignment of nodes 7, 11, and 15. The first harmonic generation is the major component of the frequency dynamic responses. The second harmonic generation is significantly reduced comparing to the experimental scheme of 0.4 mm parallel misalignment and 0.5° angular misalignment.

In comparison to the mathematical model, the experimental dynamic response curves have an oscillating behavior, especially in the first two dominant harmonic generations. That can be related to the simplified model and non-linear friction, which presents small variations all along the meshing process. The effects of these variations are considered negligible with respect to the effects induced by the torsional and dynamic vibration of the meshing process, and that can be the subject of future papers.

5. Conclusions

The dynamic characteristics of misalignment and contact tooth analysis are studied in this paper, combining theoretical and experimental approaches. Firstly, a dynamic analysis for propulsion shaft system of marine is carried out, and the motion differential equation is developed by Euler–Bernoulli beam model. Then, the meshing state, geometrics, and contact tooth analysis considering parallel and angular misalignment of gear coupling are analyzed, and the comprehensive meshing force model of gear coupling is presented. In combination with the contact force modeling of bearing, the complete dynamic equation can be obtained. Furthermore, the GCRS is divided into several nodes and elements by the structural analysis, and the dynamic equation of GCRS can be solved based on Newmark integration method. The dynamic characteristics and vibration shapes are analyzed with variation bearing stiffness and misalignment. The mathematical simulation results show that both parallel and angular misalignment can induce the second harmonic generation, and the influence of angular misalignment is more significant than that of parallel misalignment.

Finally, the experimental test of dynamic characteristics for GCRS is carried out by a reduced-scale propulsion shaft system, and the first four natural frequencies and dynamic responses are analyzed by vibration monitoring analyzer. In comparison to the mathematical simulation results, the experimental results validate the similarity of variation trend and rule of each order harmonic generations, which demonstrate the meshing model and dynamic equation, can represent the actual operation of GCRS.

The main contribution of this paper is the dynamic characteristics analysis scheme for GCRS. The modeling method and experimental test have been validated by the vibration detection system, which can be used to the industry machine tools. The proposed analysis method of dynamic characteristics is suitable for complex shafting and can be further extended to the propeller–shaft–hull coupled system of marine.

Author Contributions: Conceptualization, W.F.; methodology, W.F.; project administration, H.L.; software, Y.Z.; validation, X.S. and W.F. All authors have read and agreed to the published version of the manuscript.

Conflicts of Interest: The authors declare no conflict of interest.

References

1. Cuffaro, V.; Cura, F.; Mura, A. Analysis of the pressure distribution in spline couplings. *Proc. Inst. Mech. Eng. Part C J. Mech. Eng. Sci.* **2012**, *226*, 2852–2859. [CrossRef]
2. Su, J.Z.; Yang, X.H.; Guan, Y.B.; Liu, G.L. Finite elements analysis of large marine crown gear coupling. *J. Mech. Trans.* **2017**, *41*, 64–66.
3. Yabin, G.; Zongde, F.; Xiaohui, Y.; Guoding, C. Tooth contact analysis of crown gear coupling with misalignment. *Mech. Mach. Theory* **2018**, *126*, 295–311.
4. Yuanqiang, T.; Jianfa, H.; Shengqiang, J. Research of misaligned load distribution of involute spline pair based on finite element method. *J. Mech. Transm.* **2016**, *9*, 110–113.
5. Al-Hussain, K.M. Dynamic stability of two rigid rotors connected by a flexible coupling with angular misalignment. *J. Sound Vib.* **2003**, *266*, 217–234. [CrossRef]
6. Barrot, A.; Paredes, M.; Sartor, M. Determining both radial pressure distribution and torsional stiffness of involute spline couplings. *Proc. Inst. Mech. Eng. Part. C J. Mech. Eng. Sci.* **2006**, *220*, 1727–1738. [CrossRef]
7. Hong, J.; Talbot, D.; Kahraman, A. A semi-analytical load distribution model for side-fit involute splines. *Mech. Mach. Theory* **2014**, *76*, 39–55. [CrossRef]
8. Su, X.; Lu, H.; Zhang, X.; Fan, W.; Zhang, Y. Analysis of dynamic characteristic for misalignment-spline gear shaft based on whole transfer matrix method. *J. Vibroeng.* **2018**, *20*, 1392–1408.
9. Tian, Y.; Sun, Y.H.; Ding, C.W.; Yang, L.H.; Yu, L. Critical speeds of a high speed motor with different supports and rotor assembly. *J. Vib. Shock* **2013**, *32*, 24–30.

10. Kim, J.S.; Park, N.G.; Lee, H.W. Vibration analysis of a planetary gear system based on the transfer matrix method. *J. Mech. Sci. Tech.* **2016**, *30*, 611–621. [CrossRef]

11. Huang, B.W.; Yu, P.P.; Chen, G.S. Instability of mistuned tube-array structures with axial loads. *Nonlinear Dynam.* **2013**, *73*, 1545–1556. [CrossRef]

12. Guo, Y.; Lambert, S.; Wallen, R.; Errichello, R.; Keller, J. Theoretical and experimental study on gear-coupling contact and loads considering misalignment, torque, and friction influences. *Mech. Mach. Theory* **2016**, *98*, 242–262. [CrossRef]

13. Li, M.; Yu, L. Analysis of the coupled lateral torsional vibration of a rotor-bearing system with a misaligned gear coupling. *J. Sound Vib.* **2001**, *243*, 283–300. [CrossRef]

14. Lei, W.P.; Han, J.; Li, L.J.; Chen, L. Dynamic response analysis of the rotors connected by the misaligned gear coupling. *J. Mech. Strength* **2012**, *34*, 327–332.

15. Chen, G. Vibration modelling and verifications for whole aero-engine. *J. Sound Vib.* **2015**, *349*, 163–176. [CrossRef]

16. Archer, G.C.; Whalen, T.M. Development of rotationally consistent diagonal mass matrices for plate and beam elements. *Comput. Methods Appl. Mech. Engin.* **2005**, *194*, 675–689. [CrossRef]

17. Rincon, A.F.D.; Viadero, F.; Iglesias, M.; García, P.; De-Juan, A.; Sancibrian, R. A model for the study of meshing stiffness in spur gear transmissions. *Mech. Mach. Theory* **2013**, *61*, 30–58. [CrossRef]

18. Wang, H.; Han, Q.; Luo, R.; Qing, T. Dynamic modeling of moment wheel assemblies with nonlinear rolling bearing supports. *J. Sound Vib.* **2017**, *406*, 124–145. [CrossRef]

19. Liu, J.; Wu, H.; Shao, Y. A theoretical study on vibrations of a ball bearing caused by a dent on the races. *Engin. Fail. Anal.* **2017**, *83*, 220–229. [CrossRef]